

Magnetocaloric effect for the topological semimetal $\text{Co}_3\text{Sn}_2\text{S}_2$ due to the antiferromagnetic coupling of the bulk and surface spin-polarized phases

N.N. Orlova,¹ V.D. Esin,¹ A.V. Timonina,¹ N.N. Kolesnikov,¹ and E.V. Deviatov¹

¹*Institute of Solid State Physics of the Russian Academy of Sciences,
Chernogolovka, Moscow District, 2 Academician Ossipyan str., 142432 Russia*

(Dated: October 8, 2024)

We experimentally investigate magnetocaloric effect for the topological magnetic Weyl semimetal $\text{Co}_3\text{Sn}_2\text{S}_2$ in a wide temperature range. The isothermal magnetic entropy change ΔS is calculated from the experimental magnetization curves by using Maxwell relation. In addition to the expected ΔS peak at the Curie temperature T_C , we obtain another one at the temperature T_{inv} of the hysteresis inversion, which is the main experimental result. The inverted hysteresis usually originates from the antiferromagnetic coupling between two magnetic phases. For $\text{Co}_3\text{Sn}_2\text{S}_2$ topological magnetic Weyl semimetal these phases are the ferromagnetic bulk and the spin-polarized topological surface states. Thus, the pronounced magnetocaloric effect at T_{inv} is determined by the bulk magnetization switching by the exchange bias field of the surface spin-polarized phase, in contrast to the ferromagnetic-paramagnetic transition at the Curie temperature T_C . For possible applications of magnetocaloric effect, Weyl semimetals open a new way to shift from ferromagnetic to the antiferromagnetic systems without loss of efficiency, but with higher reversibility and with smaller energy costs.

PACS numbers: 71.30.+h, 72.15.Rn, 73.43.Nq

INTRODUCTION

The nontrivial properties of topological semimetals originate from the existence of distinct band-touching Dirac points in the bulk electronic spectrum. Weyl semimetals are also characterized by broken inversion or time-reversal symmetries, so every Dirac point is split into two Weyl nodes with opposite chiralities [1]. As a result, Fermi-arc surface states are formed as the arcs between the projections of Weyl nodes on the surface Brillouin zone [1, 2].

Among the magnetic Weyl semimetals, kagome-lattice ferromagnet $\text{Co}_3\text{Sn}_2\text{S}_2$ is a typical example hosting spin-polarized Fermi arc surface states [3]. The giant anomalous Hall effect has been reported [4, 5] for $\text{Co}_3\text{Sn}_2\text{S}_2$, as a sign of a magnetic Weyl phase [1]. Fermi arcs were directly visualized by scanning tunneling spectroscopy [2]. Spin-polarized surface textures have also been experimentally shown [6] for $\text{Co}_3\text{Sn}_2\text{S}_2$ as well as for other magnetic topological semimetals [7, 8], as a result of the spin-momentum locking in the topological Fermi-arc surface states [1].

For $\text{Co}_3\text{Sn}_2\text{S}_2$, usual rectangular ferromagnetic hysteresis is changed to the inverted one [9] at the 140 K transition temperature, demonstrating the presence of the second magnetic phase [10]. Antiferromagnetic coupling between the magnetic phases provides the exchange bias field, which facilitates the magnetization switching [11–13]. While the first phase is obviously the ferromagnetic bulk, the surface spin textures should be regarded as the second magnetic phase in magnetic topological semimetals. Due to the topological protection, the surface magnetic phase shows excellent temperature

stability, as it has been confirmed by first order reversal curve analysis and the bow-tie [14] hysteresis loops at high temperatures [9]. The described two-phase behavior is quite universal for different magnetic topological semimetals, e.g. for $\text{Co}_3\text{Sn}_2\text{S}_2$ and Fe_3GeTe_2 , only the characteristic temperatures differ for these materials [9].

For the ferromagnets, the magnetocaloric effect (MCE) is of special interest due to the possible applications [15, 16]. It is expected that the MCE-based refrigerators will be energetically more efficient than the usual ones [17]. Thus, different MCE variations are of extensive investigation nowadays, e.g. multicaloric effect [18–20], the giant magnetocaloric effect [21, 22], and the rotating magnetocaloric effect [23]. For the topological Weyl semimetal $\text{Co}_3\text{Sn}_2\text{S}_2$, usual magnetocaloric effect has been demonstrated around the Curie temperature [24, 25], as well as the rotating magnetocaloric effect [23] due to the large magnetic anisotropy [23].

The magnetocaloric effect appears as the entropy change ΔS while the system undergoes the transition between differently ordered state, usually, ferromagnetic-paramagnetic transition at the Curie point. On the other hand, the bulk magnetization switching by the exchange bias field of the surface spin-polarized phase [9] should also be accompanied by the magnetic entropy change ΔS in magnetic topological semimetals. In other words, surface-induced magnetocaloric effect can be expected for magnetic topological semimetals, which is worth the experimental investigation. For possible applications of the magnetocaloric effect, utilizing of antiferromagnetic coupling between the surface and bulk phases should increase energy efficiency of a refrigerator.

Here, we experimentally investigate magnetocaloric

effect for the topological magnetic Weyl semimetal $\text{Co}_3\text{Sn}_2\text{S}_2$ in a wide temperature range. The isothermal magnetic entropy change ΔS is calculated from the experimental magnetization curves by using Maxwell relation. In addition to the expected ΔS peak at the Curie temperature T_C , we obtain another one at the temperature T_{inv} of the hysteresis inversion, which is the main experimental result.

SAMPLES AND TECHNIQUES

$\text{Co}_3\text{Sn}_2\text{S}_2$ single crystals were grown by the gradient freezing method. Initial load of high-purity elements taken in stoichiometric ratio was slowly heated up to 920°C in the horizontally positioned evacuated silica ampule, held for 20 h and then cooled with the furnace to the ambient temperature at the rate of 20 degree/h. The obtained ingot was cleaved in the middle part. Electron probe microanalysis of cleaved surfaces and X-ray diffractometry of powdered samples confirmed stoichiometric composition and the space group $R\bar{3}m$ (No. 166) of the crystal. Since the Laue patterns confirm the hexagonal structure with (0001) as cleavage plane, we use small $\text{Co}_3\text{Sn}_2\text{S}_2$ flakes, which are obtained by a mechanical cleavage from the initial single crystal.

The experimental magnetization curves have been obtained by the Lake Shore Cryotronics 8604 VSM magnetometer. It is equipped with nitrogen flow cryostat for measurements from the room temperature down to 80 K, while the Curie temperature is known [26, 27] to be about 173 K for $\text{Co}_3\text{Sn}_2\text{S}_2$ ferromagnet. A flake is mounted to the magnetometer sample holder by a low temperature grease, which has been tested to have a negligible magnetic response. The sample can be rotated in magnetic field, so the hard and easy magnetization directions (i.e. sample orientation) can be obtained from angle-dependent magnetization.

We investigate the magnetocaloric effect as the isothermal magnetic entropy change ΔS which is calculated from the experimental magnetization curves by using Maxwell relation [28, 29]:

$$\Delta S = \mu_0 \int_0^H \left(\frac{\partial M}{\partial T} \right)_H dH \quad (1)$$

As a first step, a set of $M(H, T = \text{const})$ isotherms is obtained for the required magnetic field range. Subsequently, the first derivative $\left(\frac{\partial M}{\partial T} \right)_H$ is calculated as a result of subtraction $\left(\frac{\Delta M}{\Delta T} \right)(H, T)$ of every two neighbor curves. As a final step, ΔS is achieved for every temperature point by integration over the magnetic field range [28].

Before any set of $M(H, T = \text{const})$ isotherms, it is necessary to set up the stable initial magnetic state of

the sample. In our experiment, it is performed by cooling the sample in zero magnetic field (ZFC protocol) from the room temperature to 80 K one, and subsequent sample magnetization along the easy axis by sweeping the field between -15 kOe and +15 kOe values. Afterward, the external field is switched to zero, so the temperature is always stabilized at zero field for every $M(H, T = \text{const})$ isotherm.

EXPERIMENTAL RESULTS

Fig. 1 (a) shows hysteresis loops for a 1.42 mg $\text{Co}_3\text{Sn}_2\text{S}_2$ flake at three different temperatures, 130 K, 140 K, and 150 K, respectively. Because of the excellent reproducibility of the magnetization results from different $\text{Co}_3\text{Sn}_2\text{S}_2$ flakes [9], below we present the data from this sample only. The curves are obtained after zero-field cooling, the magnetic field is normal to the (0001) cleavage plane, i.e. it is directed along the $\text{Co}_3\text{Sn}_2\text{S}_2$ easy axis. The sample orientation is verified by the angle dependence of magnetization in Fig. 1 (b).

Hysteresis loops are of strictly rectangular shape with step-like magnetization switchings below 130 K, which confirms the single domain magnetic state of bulk $\text{Co}_3\text{Sn}_2\text{S}_2$, see Fig. 1 (a), and Ref. [9] for details. At higher temperatures, coercivity is diminishing, the slanted sections appear, so one can see a bow-tie [14] hysteresis loop at 140 K in Fig. 1 (a). Above 150 K, step-like magnetization switchings occur before the magnetic field inversion, which is known as inverted hysteresis [11–13]. The inverted hysteresis originates from antiferromagnetic coupling between the magnetic phases [11–13], which provides the exchange bias field. For $\text{Co}_3\text{Sn}_2\text{S}_2$, two phases has been directly demonstrated by FORC analysis [9].

Fig. 1 (c) shows temperature-dependent magnetization as two pairs of $M(T)$ curves. One pair is obtained in zero magnetic field after zero-field cooling and the initial sample magnetization, as it is described in the Samples section. While increasing the temperature, the inverted hysteresis transition appears as a sharp drop of magnetization at transition temperature $T_{inv} = 140$ K, see Fig. 1 (c). At higher temperatures, the transition to the paramagnetic state can be identified at $T_C = 173$ – 175 K in the inset to Fig. 1 (c), which well corresponds to the known $\text{Co}_3\text{Sn}_2\text{S}_2$ Curie temperature [26, 27]. The backward zero-field cooling $M(T)$ curve shows negligible magnetization value, as it should be expected for a ferromagnet while going from above the Curie temperature. For the second pair of $M(T)$ curves, both cooling and heating (FC/FH protocols) are performed at 5 kOe magnetic field. For both FC/FH curves, magnetization drops to zero at the Curie temperature T_C . In the FC case, 5 kOe magnetic field is applied at 190 K $> T_C$ temperature along the easy magnetization axis, with subsequent cooling to 130 K. Since 5 kOe magnetic field is

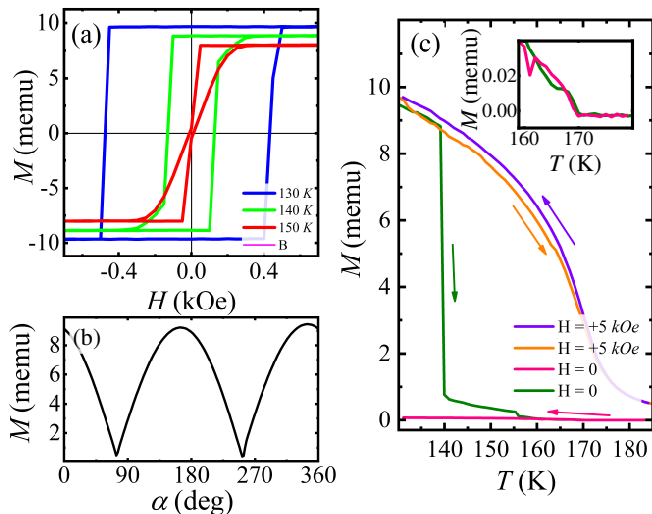


Figure 1. (Color online) (a) Examples of hysteresis loops for a 1.42 mg $\text{Co}_3\text{Sn}_2\text{S}_2$ flake for different temperatures around the T_{inv} . The loops are of strictly rectangular shape with step-like magnetization switchings at 130 K and below, which confirms the single domain magnetic state of the $\text{Co}_3\text{Sn}_2\text{S}_2$ flake. At 140 K, the slanted hysteresis sections appear, so the loop is of bow-tie type [14]. At 150 K and for high temperatures, step-like magnetization switchings occur before the magnetic field inversion, which is known as inverted hysteresis [11–13]. The curves are obtained after zero-field cooling, the magnetic field is along the $\text{Co}_3\text{Sn}_2\text{S}_2$ easy axis direction. (b) Angle dependence of magnetization M for the $\text{Co}_3\text{Sn}_2\text{S}_2$ single crystal flake. The curve is obtained at 5 kOe magnetic field, i.e. for fully saturated sample magnetization. (c) Temperature-dependent sample magnetization $M(T)$. Green and pink curves are obtained in zero magnetic field after zero-field cooling and the initial sample magnetization, see the Samples section. While increasing the temperature, the inverted hysteresis transition appears as a sharp drop of magnetization at $T_{inv} = 140$ K. The backward zero-field cooling $M(T)$ curve shows negligible magnetization value. For the orange and purple $M(T)$ curves, both cooling and heating are performed at 5 kOe magnetic field (FC/FH protocols). The curves are smooth, without any peculiarity at $T_{inv} = 140$ K, and with negligible difference for the FC and FH curves. Inset shows the enlarged region around the Curie temperature $T_C = 173$ – 175 K for the zero-field cooling and heating curves.

well above the inverted hysteresis region in Fig. 1 (a), the curves are smooth, without any peculiarity at $T_{inv} = 140$ K, and with negligible difference for the FC and FH curves.

For the magnetocaloric effect investigation, $M(H, T = const)$ isothermal magnetization curves are obtained in a wide temperature range, to cover both the Curie temperature T_C and the inversion transition T_{inv} , see Fig. 2 (a). Since magnetocaloric effect is well studied near the Curie temperature [24, 25], it can be regarded as a reference to confirm the correctness of our procedure. The initial sample state is obtained after ZFC from room temperature to 80 K with subsequent magnetization in the

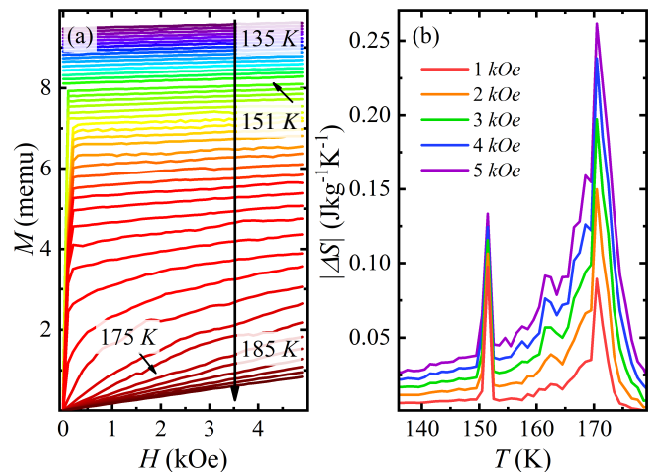


Figure 2. (Color online) (a) $M(H, T = const)$ isothermal magnetization curves in a wide temperature range from 135 K to 185 K with 1 K step. The initial sample state is obtained after ZFC from room temperature to 80 K with subsequent sample magnetization, see the Samples section. (b) The absolute value of the isothermal magnetic entropy change $|\Delta S|$ as obtained from Eq.(1), for different limits of the magnetic field H . In addition to the known [23–25] $|\Delta S|$ peak at the Curie temperature T_C , we obtain another one at the inversion point T_{inv} , which is the main experimental result. The peaks’ amplitudes are comparable at both temperatures, T_C and T_{inv} .

external field up to ± 15 kOe, as described above. Afterward, temperature is stabilized in zero field with 1 K step, $M(H)$ curves are obtained from 135 K to 185 K, see Fig. 2 (a).

The isothermal magnetic entropy change ΔS can be calculated by Eq.(1) for different limits of the magnetic field H , absolute $|\Delta S|$ values are presented in Fig. 2 (b). For the widest field range (up to 5 kOe), the obtained $|\Delta S|$ behavior well correspond to the known [23–25] for $\text{Co}_3\text{Sn}_2\text{S}_2$: Fig. 2 (b) shows $|\Delta S(T)| = 0.26 \text{ J} \times \text{kg}^{-1} \times \text{K}^{-1}$ around the Curie temperature T_C , similarly to Ref. [25]. The $|\Delta S|$ peak value is linearly diminishing for narrower field ranges, while the qualitative behavior is the same, see Fig. 2 (b).

As the main experimental result, Fig. 2 (b) shows narrow $|\Delta S|$ peak at the inversion temperature T_{inv} , in addition to the $|\Delta S|$ peak around the Curie point. The peaks’ amplitudes are comparable at both temperatures, T_C and T_{inv} . Due to the abrupt changes in $M(H, T)$ at the T_{inv} transition point in Fig. 1 (a) and (c), the detailed measurements are required with smaller temperature step to avoid the $|\Delta S|$ peak smoothing around the T_{inv} .

Fig. 3 (a) shows $M(H, T = const)$ isothermal magnetization curves for the narrow 145 – 155 K temperature interval with 0.3 K step. The curves are obtained after initial ZFC with subsequent magnetization, similarly to ones in Fig. 2 (a). The calculated $|\Delta S|$ is de-

picted in Fig. 3 (d) as a red curve for the 5 kOe magnetic field range, while the reference blue one is from Fig. 2 (b). The $|\Delta S|$ peak at T_{inv} is even narrower for the smaller temperature step, the peak height is of the same $|\Delta S(T)| \approx 0.3 \text{ J} \times \text{kg}^{-1} \times \text{K}^{-1}$ value as at the Curie temperature T_C . Thus, the magnetocaloric effect is of the same value for the ferromagnetic-paramagnetic transition at T_C and for inverted hysteresis transition at much lower temperature T_{inv} .

However, the position of the inversion point T_{inv} varies from cooling to cooling, as it can be seen from red and blue curves in Fig. 3 (d). Being determined by interaction of two magnetic phases, T_{inv} is mostly affected by the bulk coercivity value, since the topological surface phase is of excellent stability [9]. For a particular $\text{Co}_3\text{Sn}_2\text{S}_2$ single crystal with definite shape and size, the bulk coercivity varies due to the stress and defects redistribution in different cooling cycles, leading to T_{inv} within 140–151 K temperature interval.

Due to the observed T_{inv} variation, the stability of the obtained results for $|\Delta S|$ should be demonstrated by measurements with different, e.g. field-cooling protocol. Fig. 3 (b) shows $M(H, T = \text{const})$ isothermal magnetization curves for the 143 – 153 K temperature interval with 0.5 K step. The curves are obtained after the initial cooling at 5 kOe magnetic field (FC protocol). (c) $M(H, T = \text{const})$ isothermal magnetization curves around the Curie temperature T_C after the field cooling at 5 kOe. (d) The calculated absolute value of the isothermal magnetic entropy change $|\Delta S|$ is depicted in Fig. 3 (d) as a green curve. The result is qualitatively similar to the ZFC case: the $|\Delta S|$ peak is of approximately same height, it is wider due to the increased temperature step, while the peak position is considerably changed since coercivity is always smaller in the FC case.

As a reference, we reproduce $M(H, T = \text{const})$ isothermal magnetization curves around the Curie temperature T_C after the field cooling at 5 kOe, see Fig. 3 (c). The result of the $|\Delta S|$ calculation is shown in Fig. 3 (d) as a brown curve. The $|\Delta S|$ is of the same height as for the ZFC case, it is centered at the same T_C value. Thus, we should conclude that the magnetocaloric effect is practically insensitive to the cooling procedure and, therefore, the initial sample state around the Curie point $T_C = 173\text{--}175 \text{ K}$.

DISCUSSION

As a result, in addition to the ferromagnetic-paramagnetic transition at the Curie temperature T_C , the pronounced magnetocaloric effect is observed at much lower temperature T_{inv} , where the effect of the second magnetic phase appears as the inverted hysteresis loop. The isothermal magnetic entropy ΔS at T_{inv} is of the same $\approx 0.3 \text{ J} \times \text{kg}^{-1} \times \text{K}^{-1}$ value as at the Curie temperature T_C .

The corresponding temperature variation ΔT can be estimated [29, 30] from $\Delta S(T)$ as:

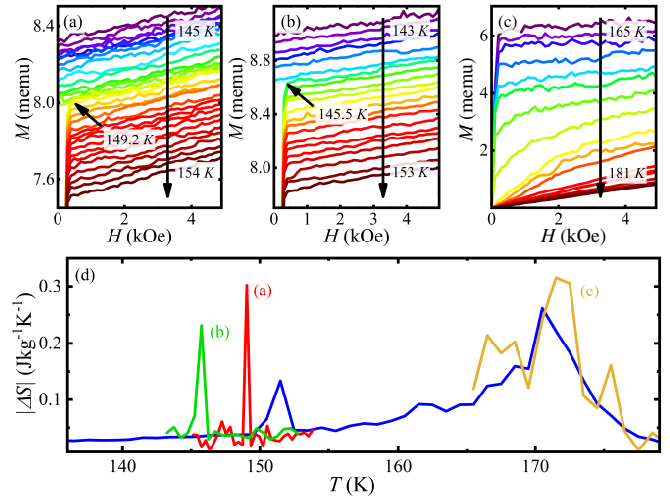


Figure 3. (Color online) (a) $M(H, T = \text{const})$ isothermal magnetization curves for the narrow 145 – 155 K temperature interval with 0.3 K step, ZFC protocol. The curves are obtained after initial ZFC with subsequent magnetization, similarly to ones in Fig. 2 (a). (b) $M(H, T = \text{const})$ isothermal magnetization curves for the 143 – 153 K temperature interval with 0.5 K step. The curves are obtained after the initial cooling at 5 kOe magnetic field (FC protocol). (c) $M(H, T = \text{const})$ isothermal magnetization curves around the Curie temperature T_C after the field cooling at 5 kOe. (d) The calculated absolute value of the isothermal magnetic entropy change $|\Delta S|$. The red, green and brown curves are obtained from the $M(H, T = \text{const})$ data, presented in (a), (b) and (c), respectively. The blue curve is a reference, it is reproduced from Fig. 2 (b) for the same 5 kOe field range. The magnetocaloric effect is practically insensitive to the initial sample state around the Curie point $T_C = 173\text{--}175 \text{ K}$, while the $|\Delta S|$ peak position depends on the the cooling procedure for inverted hysteresis transition. From the peaks' amplitudes, the magnetocaloric effect is as well efficient for inverted hysteresis transition, as for the usual ferromagnetic-paramagnetic transition at T_C .

$$\Delta T = -\frac{T\Delta S}{C_p(H)} \quad (2)$$

The $\text{Co}_3\text{Sn}_2\text{S}_2$ heat capacity C_p equals [31] to $286 \text{ J} \times \text{kg}^{-1} \times \text{K}^{-1}$ and $307 \text{ J} \times \text{kg}^{-1} \times \text{K}^{-1}$ for 147 K and 173 K, respectively. Thus, one can estimate $\Delta T \approx 0.15\text{--}0.17 \text{ K}$ for these transition points.

In principle, coexistence of two magnetic phases can be anticipated for $\text{Co}_3\text{Sn}_2\text{S}_2$ from $M(T)$ measurements in fixed magnetic fields [32–34] and from the AHE hysteresis [34]. While the first phase is obviously the ferromagnetic bulk, the existence of the second phase was explained by disorder effects [32] or even by the spin-glass state [34]. However, FORC measurements [9] directly demonstrate multi-phase behavior even at lowest temperatures, with excellent temperature stability of the second phase in comparison with the main ferromagnetic

one [9]. Also, qualitatively similar behavior is observed for $\text{Co}_3\text{Sn}_2\text{S}_2$ samples of extremely different size (two orders of magnitude in Ref. [9]), and for another magnetic topological semimetal FGT, demonstrating universal character of the second phase [9]. Thus, it can hardly be ascribed to temperature-induced disorder effects [32–34].

On the other hand, $\text{Co}_3\text{Sn}_2\text{S}_2$ is the magnetic semimetal with topologically protected Fermi-arc surface states [2, 3, 35, 36]. Due to the spin-momentum locking, one can expect skyrmion-like topological surface spin textures, as it has been confirmed experimentally for $\text{Co}_3\text{Sn}_2\text{S}_2$ magnetic Weyl semimetal [6]. Thus, one should ascribe the second, temperature-stable magnetic phase to the surface states in topological semimetals, since the surface spin textures are inherent for magnetic topological semimetals due to the spin-momentum locking in the topological surface states [9]. Also, the hysteresis loops are of the bow-tie type in Fig. 1 (a), which is usually ascribed to surface spin textures [37–41].

In this case, the magnetocaloric effect at T_{inv} is determined by the transition from the ferromagnetic bulk spin ordering to the antiferromagnetic interaction of the bulk and surface spin-polarized phases. The exchange field of the surface phase is strong enough to induce magnetization direction switching of the bulk ferromagnetic phase. In other words, isothermal magnetic entropy ΔS is determined by the reorientation of the magnetization direction for the bulk ferromagnetic phase at T_{inv} , while ΔS reflects the transition from ferromagnetic to the paramagnetic ordering at the Curie temperature T_C . Similar values of ΔS and, therefore, ΔT at both transition points in Fig. 3 (d) indicate strong influence of the surface state induced spin polarization on the bulk ferromagnetic magnetization in Weyl topological semimetals.

For possible applications of magnetocaloric effect, Weyl semimetals open a new way to transfer from ferromagnetic to the antiferromagnetic systems without loss of efficiency in ΔS and, therefore, in ΔT , but with higher reversibility and with smaller energy costs, which is confirmed by much narrower ΔS peak at T_{inv} in Fig. 3 (d).

CONCLUSION

As a conclusion, we experimentally investigate magnetocaloric effect for the topological magnetic Weyl semimetal $\text{Co}_3\text{Sn}_2\text{S}_2$ in a wide temperature range. The isothermal magnetic entropy change ΔS is calculated from the experimental magnetization curves by using Maxwell relation. In addition to the expected ΔS peak at the Curie temperature T_C , we obtain another one at the temperature T_{inv} of the hysteresis inversion, which is the main experimental result. The $|\Delta S|$ peak height is of the same $\approx 0.3 \text{ J} \times \text{kg}^{-1} \times \text{K}^{-1}$ value as at the Curie temperature T_C . Thus, the magnetocaloric effect is of

the same value for the ferromagnetic-paramagnetic transition at T_C and for inverted hysteresis transition at much lower temperatures. Similar values of ΔS and, therefore, ΔT at both transition points in Fig. 3 (d) indicate strong influence of the surface state induced spin polarization on the bulk ferromagnetic magnetization in Weyl topological semimetals.

ACKNOWLEDGEMENT

We wish to thank S.S Khasanov for X-ray sample characterization.

-
- [1] N.P. Armitage, E.J. Mele, and A. Vishwanath, *Rev. Mod. Phys.* 90, 015001 (2018).
 - [2] Noam Morali, Rajib Batabyal, Pranab Kumar Nag, Enke Liu, Qiunan Xu, Yan Sun, Binghai Yan, Claudia Felser, Nurit Avraham, Haim Beidenkopf, *Science* Vol.365, 1286–1291 (2019). doi:10.1126/science.aav2334
 - [3] S. Albarakati, C. Tan, Z. Chen, J. G. Partridge, G. Zheng, L. Farrar, E. L. H. Mayes, M. R. Field, C. Lee, Y. Wang, Y. Xiong, M. Tian, F. Xiang, A. R. Hamilton, O. A. Tretiakov, D. Culcer, Y. Zhao, and Y. Wang, *Sci. Adv.* 5, eaaw0409 (2019). <https://doi.org/10.1126/sciadv.aaw0409>
 - [4] Enke Liu, Yan Sun, Nitesh Kumar, Lukas Muechler, Aili Sun, Lin Jiao, Shuo-Ying Yang, Defa Liu, Aiji Liang, Qiunan Xu, Johannes Kroder, Vicky Süß, Horst Borrmann, Chandra Shekhar, Zhaosheng Wang, Chuanying Xi, Wenhong Wang, Walter Schnelle, Steffen Wirth, Yulin Chen, Sebastian T. B. Goennenwein, and Claudia Felser, *Nature Physics* 14, 1125 (2018)
 - [5] Qi Wang, Yuanfeng Xu, Rui Lou, Zhonghao Liu, Man Li, Yaobo Huang, Dawei Shen, Hongming Weng, Shancai Wang and Hechang Lei, *Nature Communications* 9, 3681 (2018)
 - [6] Akira Sugawara, Tetsuya Akashi, Mohamed A. Kassem, Yoshikazu Tabata, Takeshi Waki, and Hiroyuki Nakamura, *Physical Review Materials* 3, 104421 (2019).
 - [7] Myung-Geun Han, Joseph A. Garlow, Yu Liu, Huiqin Zhang, Jun Li, Donald DiMarzio, Mark W. Knight, Cedimir Petrovic, Deep Jariwala and Yimei Zhu, *Nano Lett.*, 19, 11, 7859 (2019).
 - [8] Bei Ding, Zefang Li, Guizhou Xu, Hang Li, Zhipeng Hou, Enke Liu, Xuekui Xi, Feng Xu, Yuan Yao, and Wenhong Wang, *Nano Lett.*, 20, 868–873 (2020).
 - [9] A.A. Avakyan, N.N. Orlova, A.V. Timonina, N.N. Kolesnikov, E.V. Deviatov, *Journal of Magnetism and Magnetic Materials*, Vol. 573, p. 170668 (2023) <https://doi.org/10.1016/j.jmmm.2023.170668>
 - [10] M. Charilaou, C. Bordel, and F. Hellman, *Appl. Phys. Lett.* 104, 212405 (2014).
 - [11] J. Nogués, Ivan K. Schuller, *Journal of Magnetism and Magnetic Materials*, 192, 203 (1999).
 - [12] M. J. O’Shea and A.-L. Al-Sharif, *Journal of Applied Physics* 75, 6673 (1994).
 - [13] Mohammad Saghayezhian, Zhen Wang, Hangwen Guo, Rongying Jin, Yimei Zhu, Jiandi Zhang and E. W. Plum-

- mer Physical Review Research 1, 033160 (2019).
- [14] Felipe Tejo, Denilson Toneto, Simón Oyarzún, José Hermosilla, Caroline S. Danna, Juan L. Palma, Ricardo B. da Silva, Lucio S. Dorneles, and Juliano C. Denardin, *ACS Appl. Mater. Interfaces*, 12, 47, 53454 (2020).
- [15] Altifani Rizky Hayyu, Stanislaw Baran and Andrzej Szytula, (2024) arXiv:2402.17912v1
- [16] Julia Lyubina, *Journal of Physics D: Applied Physics* Vol. 50, 053002 (2017)
- [17] V. Franco, J.S. Blazquez, J.J. Ipus, J.Y. Law, L.M. Moreno-Ramirez, A. Conde, *Progress in Materials Science*, Vol. 93, 112–232 (2018)
- [18] Melvin M. Vopson, Yuri K. Fetisov, Ian Hepburn, *Magnetochemistry* 7, 12, 154 (2021) <https://doi.org/10.3390/magnetochemistry7120154>
- [19] Jia-Zheng Hao, Feng-Xia Hu, Zi-Bing Yu, Fei-Ran Shen, Hou-Bo Zhou, Yi-Hong Gao, Kai-Ming Qiao, Jia Li, Cheng Zhang, Wen-Hui Liang, Jing Wang, Jun He, Ji-Rong Sun and Bao-Gen Shen, *Chin. Phys. B* Vol. 29, No. 4 047504 (2020).
- [20] X. Wan, A. M. Turner, A. Vishwanath, S. Y. Savrasov, *Phys. Rev. B* 83, 205101 (2011).
- [21] H. Chouaibi, S. Mansouri, S. Aitjmal, M. Balli, O. Chdil, M. Abbasi Eskandari, S. H. Bukhari, P. Fournier (2024), arXiv:2401.01431
- [22] Pedro Baptista de Castro, Kensei Terashima, Takafumi D. Yamamoto, Suguru Iwasaki, Ryo Matsumoto, Shintaro Adachi, Yoshito Saito, Hiroyuki Takeya and Yoshihiko Takano *Science And Technology Of Advanced Materials*, 21, NO. 1, 849 (2020) <https://doi.org/10.1080/14686996.2020.1856629>
- [23] Anzar Ali, Shama, Yogesh Singh, *J. Appl. Phys.* 126, 155107 (2019). <https://doi.org/10.1063/1.5120005>
- [24] Qi Shia, Xiao Zhanga, En Yanga, Jin Yana, Xiaoyun Yua, Chang Suna, Si Lib, Zhengwei Chen, *Results in Physics*, Vol. 11, pp. 1004–1007 (2018). <https://doi.org/10.1016/j.rinp.2018.10.027>
- [25] Jiyu Hu, Xucai Kan, Zheng Chen, Ganhong Zheng, Yongqing Ma, *Journal of the American Ceramic Society*, 105, pp 4827–4839 (2022). DOI: 10.1111/jace.18465.
- [26] W. Schnelle, A. Leithe-Jasper, H. Rosner, F. M. Schapacher, R. Pöttgen, F. Pielhofer, and R. Wehrich, *Phys. Rev. B* Vol. 88, 144404 (2013)
- [27] Mohamed A. Kassem, Yoshikazu Tabata, Takeshi Waki and Hiroyuki Nakamura *Phys. Rev. B* Vol. 96, 014429 (2017)
- [28] V. Franco, Lake Shore Cryotronics, Inc. | t. 614.891.2243 | f. 614.818.1600 | www.lakeshore.com
- [29] Tishin, A.M. and Spichkin, Y.I. (2003). *The Magnetocaloric Effect and its Applications* (1st ed.). CRC Press. <https://doi.org/10.1201/9781420033373>
- [30] M. Földeáki, R. Chahine; T. K. Bose *J. Appl. Phys.* 77, 3528–3537 (1995), doi.org/10.1063/1.358648
- [31] W. Schnelle, A. Leithe-Jasper, and H. Rosner, *Physical Review B*, Vol. 88, 144404 (2013)
- [32] Z. Guguchia, J. A. T. Verezhak, D. J. Gawryluk, S. S. Tsirkin, J.-X. Yin, I. Belopolski, H. Zhou, G. Simutis, S.-S. Zhang, T. A. Cochran, G. Chang, E. Pomjakushina, L. Keller, Z. Skrzeczkowska, Q. Wang, H. C. Lei, R. Khasanov, A. Amato, S. Jia, T. Neupert, H. Luetkens and M. Z. Hasan, *Nature Communications*, 11, 559 (2020).
- [33] H.C. Wu, P.J. Sun, D.J. Hsieh, H.J. Chen, D. Chandrasekhar Kakarla, L.Z. Deng, C.W. Chu, H.D. Yang, *Materials Today Physics*, 12, 100189 (2020).
- [34] Ella Lachman, Ryan A. Murphy, Nikola Maksimovic, Robert Kealhofer, Shannon Haley, Ross D. McDonald, Jeffrey R. Long and James G. Analytis, *Nature Communications*, 11, 560 (2020).
- [35] Noam Morali, Rajib Batabyal, Pranab Kumar Nag, Enke Liu, Qiunan Xu, Yan Sun, Binghai Yan, Claudia Felser, Nurit Avraham, Haim Beidenkopf, *Science* 365, 1286 (2019).
- [36] Qi Wang, Yuanfeng Xu, Rui Lou, Zhonghao Liu, Man Li, Yaobo Huang, Dawei Shen, Hongming Weng, Shancai Wang and Hechang Lei, *Nature Communications*, 9, 3681 (2018).
- [37] Robert Streubel, Luyang Han, Mi-Young Im, Florian Kronast, Ulrich K. Röler, Florin Radu, Radu Abrudan, Gungun Lin, Oliver G. Schmidt, Peter Fischer and Denys Makarov, *Scientific Reports*, 5, 8787 (2015).
- [38] Senfu Zhang, Junwei Zhang, Yan Wen, Eugene M. Chudnovsky and Xixiang Zhang, *Communications Physics*, 1, 36 (2018).
- [39] Senfu Zhang, Junwei Zhang, Qiang Zhang, Craig Barton, Volker Neu, Yuelei Zhao, Zhipeng Hou, Yan Wen, Chen Gong, Olga Kazakova, Wenhong Wang, Yong Peng, Dmitry A. Garanin, Eugene M. Chudnovsky and Xixiang Zhang, *Applied Physics Letters* 112, 132405 (2018).
- [40] You Ba, Shihao Zhuang, Yike Zhang, Yutong Wang, Yang Gao, Hengan Zhou, Mingfeng Chen, Weideng Sun, Quan Liu, Guozhi Chai, Jing Ma, Ying Zhang, Huanfang Tian, Haifeng Du, Wanjun Jiang, Cewen Nan, Jia-Mian Hu and Yonggang Zhao, *Nature Communications*, 12, 322 (2021); <https://doi.org/10.1038/s41467-020-20528-y>.
- [41] Anjan Soumyanarayanan, M. Raju, A. L. Gonzalez Oyarce, Anthony K. C. Tan, Mi-Young Im, A. P. Petrović, Pin Ho, K. H. Khoo, M. Tran, C. K. Gan, F. Ernult and C. Panagopoulos, *Nature Mater*, 16, 898E–904 (2017). <https://doi.org/10.1038/nmat4934>.